The impact of rheology on the transition from stick-slip to creep in a semi-brittle analog

T. Birren[1] and J. E. Reber[1]

[1]Department of Geological and Atmospheric Sciences, Iowa State University, Ames, IA 50011

Corresponding author: Thomas Birren (tbirren@iastate.edu)

Key Points:

- Yield stress controls the slip dynamics in semi-brittle analog materials during simple shear.
- The propagation and interaction of opening (mode I) and shear (mode II) fractures can be linked to different slip dynamics ranging from stick-slip to creep.

Abstract

Faults can release energy via a variety of different slip mechanisms ranging from steady creep to fast and destructive earthquakes. Tying the rheology of the crust to various slip dynamics is important for our understanding of plate tectonics and earthquake generation. Here, we propose that the interplay of fractures and viscous flow leads to a spectrum between stick-slip and creep. We use an elasto-visco-plastic rock analog (Carbopol U-21) where we vary the yield stress to investigate its impact on slip dynamics in shear experiments. The experiments are performed using a simple shear apparatus, which provides distributed shear across the entire width of the experiment and allows in situ observations of deformation. We record force and displacement during deformation and use time lapse photography to document fracture development. A low yield stress (25 Pa) leads to creep dynamics in the absence of fractures. An intermediate yield stress (144 Pa) leads to the development and interaction of opening (mode I) and shear (mode II) fractures. This interaction leads to a spectrum in slip dynamics ranging from creep to stick-slip. A high yield stress (357 Pa) results in the development of many mode I fractures and a deformation signal dominated by stick-slip. These results show that bulk yield stress, fracture formation, and slip dynamics are closely linked and can lead to a continuum between creep and stick-slip. We suggest that rheology should be considered as an additional mechanism to explain the broad range of slip dynamics in natural faults.

Key words: Slip dynamics, Carbopol, Semi-brittle, Analog experiments

1 Introduction

Fault zones release stored elastic energy with various intensities and at different time scales. Some faults creep steadily (e.g., Burgmann et al., 2000; Thatcher, 2009), some slowly and periodically releasing energy as “slow earthquakes” (e.g., Beroza and Ide, 2011), and some abruptly release large amounts of energy manifested as earthquakes (e.g., Kanamori, 1994). Constraining the rheological behavior and slip dynamics of faults is of fundamental importance for the understanding of plate tectonics as well as earthquake generation. However, this task is difficult because lithosphere-scale fault zones cross-cut many lithologies and operate over broad ranges of pressure, temperature, and strain rates. Therefore, several deformation processes contribute to the overall strength of the lithosphere. Geologic observations indicate that brittle and ductile deformation processes occur simultaneously in time and space, leading to a semi-brittle bulk behavior (Fagereng and Sibson, 2010; Hayman and Lavier, 2014; Mancktelow and Pennacchioni, 2005). During semi-brittle deformation, some phases deform in a brittle manner, which is manifested by the loss of cohesion and the formation of fractures. At the same time, other phases deform in a ductile manner where no fractures form. This co-existantce of brittle and ductile deformation processes has the potential to not only impact deformation localization but also deformation dynamics (Figure 1). Semi-brittle materials combine deformation time scales associated with fractures and earthquakes and those associated with the flow of the ductile crust, which could potentially explain some observed strain transients and slow slip (Burgmann, 2018; Peng and Gomberg, 2010; Wech and Creager, 2011). Note that henceforth, we are using the term ‘stick-slip’ not sensu stricto as a frictional behavior on an existing surface (Scholz, 1990) but in a broader sense where a period of locking and stress build up is followed by subsequent slip.

Semi-brittle deformation is abundant in nature; its effects are observed in granitic mylonites (e.g., Fitz Gerald and Stunitz, 1993; Gapais, 1989; Handy, 1990; Simpson, 1985; Stunitz and Fitz Gerald, 1993; Viegas et al., 2016), in accretionary prism sediments (Fagereng and Harris, 2014; Fagereng and Sibson, 2010), and in shear zones (Hayman and Lavier, 2014; Mancktelow, 2006) and are observed on scales ranging from micrometers to kilometers (e.g., Carreras, 2001; Handy, 1990). Field observations led Fagereng and Sibson (2010) to hypothesize that the partitioning between a weak, viscous phase and a competent, brittle phase in an accretionary prism may affect seismicity during subduction. Experimental work on granular-fluid material mixtures has shown a similar transition from stick-slip to creep dynamics depending on the presence and viscosity of a weak, fluid phase (Higashi and Sumita, 2009; Reber et al., 2014). The overall idea is that an abundant viscous fluid phase would lead to a creep signal, whereas an abundant brittle phase would lead to a stick-slip signal. The impact of a semi-brittle rheology on the transition between creep and stick-slip has been investigated in a number of physical experiments (Burton et al., 2018; Moore, 2014; Reber et al., 2015) as well as theoretical (Lavier et al., 2013) and numerical (Jammes et al., 2015; Webber et al., 2018) studies.

Here, we present results from analog experiments using a semi-brittle model material where we can vary the yield stress. Analog experiments provide unparalleled opportunities to observe, in situ, the contributions of brittle and ductile processes to deformation without describing the deformation process a priori. We link the macroscopic deformation structures to slip dynamics to investigate the impact of the yield stress of a semi-brittle model material on evolving fracture patterns and related deformation dynamics.

2 Methods

2.1 Experimental Apparatus

The experiments are conducted on a simple shear apparatus in which the shear deformation is distributed over the entire width of the experimental table (Figure 2). One side of the table remains stationary while the other side is free to move on four roller bearings in a linear track. The surface is made up of 34 parallel acrylic strips that move independently in simple shear like a deck of cards (Schreurs, 1994). Motion is driven by a linear stepping motor coupled to the machine by a Chatillon DFS II piezoelectric force gauge and a spring (Figure 2, inset). The spring (spring constant, k = 123 N/m) allows for a boundary condition where neither strain rate nor constant force are prescribed. Instead, the spring will elastically load the system until the force is large enough for deformation to occur. This deformation can be on a spectrum between continuous creep and stick-slip depending on the model material. All experiments are performed with the same spring. We chose a spring that is only slightly stronger than what is necessary to move the apparatus including the experiment. If a spring with a larger spring constant would be chosen the system will not be able to store elastic energy and a constant strain rate will be imposed. The apparatus can reach shear strains of $\gamma = 2$. Displacement of the free moving side is measured with a Celesco cable transducer. We sample both force and displacement at 10 Hz.

2.2 Rock analog

We use a power law yield stress fluid, Carbopol Ultrez 21, (power law exponent $n = 3$) as a rock analog (Coussot et al., 2009; Di Guiseppe et al., 2015). Carbopol is an acrylate cross-polymer gel commonly used as a rheologic modifier in personal care products such as hair gel. It is a suitable semi-brittle analog because it is made of microgel “grains” representing the brittle phase and a viscous interstitial fluid phase (Lubrizol, 2012; Reber et al., 2015; Shafiei et al., 2018). For consistent Carbopol properties, we follow a published mixing procedure (Di Giuseppe et al., 2015). Carbopol is acquired from the Lubrizol Corporation in powder form. For the model material preparation, we conducted the following steps: 1) The powdered Carbopol is allowed to "wet" in distilled water for 1 hour. 2) To ensure thorough homogeneity, the solution is mixed using a magnetic stirrer set at 150 rpm for two days. At this point the Carbopol is acidic and no cross-linking of the polymer chains has yet taken place. 3) By adding a base (18 wt.% NaOH solution), we neutralize the Carbopol. This leads to cross-linking of the polymer chains and to an almost instantaneous stiffening of the mixture. The cross-linked chains coalesce into microgel grains that are elasto-plastic and are separated by a viscous interstitial fluid (Figure S1 Supporting Infromation). The yield stress is a representative quantity of the ratio between micro-gel grains and interstitial fluid. A lower yields stress is the result of a lower concentration of micro-gel grains and is similar to a material with a dominantly viscous rheology. A high yield stress results from a greater concentration of micro-gel grains leading to a rheology that is dominantly brittle. The bulk viscosity of Carbopol can be tuned independently of the yield stress; the yield stress is adjusted by the Carbopol powder to water ratio, while the bulk viscosity is dependent on the pH of the water (Lubrizol, 2012). We perform experiments on Carbopol mixed at 1, 2, and 3 wt.% and a pH of 7, with corresponding yield stress values of 25, 144, and 357 Pa, respectively (Figure S2 Supporting Infromation).

2.3 Experiment Procedure

The rock analog is spread on the shear table in a 20 x 50 x 1 cm slab. We introduce a 7.5 cm long fracture, parallel to the shear direction, in the middle of all experiments by cutting the Carbopol with a kitchen knife. The length of the shear fracture is arbitrary but constant between all experiments. It acts as a pre-existing heterogeneity. There are two reasons for this: 1) rock exhumed from the mid-crust is observed with pre-existing joints and fractures (Mancktelow, 2008; Pennacchioni and Mancktelow, 2013) and 2) in order to concentrate fractures away from the boundaries, a heterogeneity is needed in the middle of the Carbopol (Piau, 2007; Tabuteau et al., 2011). We take time-lapse photographs of the experimental surface to reconstruct the strain field during deformation. Photographs are taken from a height of 40 cm and at an interval of 2 s. The correlation between the force and displacement measurement and the photos has an estimated error of ± 1 s.

We conducted three experiments for each of the yield stresses tested. The same batch of Carbopol is used in each set of experiments to ensure that mixing procedure and aging effects are limited (Di Giuseppe et al., 2015). While no experiments produced the exact same results, deformation dynamics at each yield stress were consistent (Figure S3 Supporting Information). Here, we chose to compare three representative experiments of different yield stress to each other.

2.4 Particle Image Velocimetry

To visualize the strain field, we employ particle image velocimetry (PIV). The Matlab application PIVlab tracks individual particles over the entire area of the experiment (Thielicke and Stamhuis, 2014a; 2014b; Thielicke, 2014). Particles displaced less than their diameter between two photographs can be tracked and a velocity map can be computed. We use bubbles near the surface of the Carbopol as trackable particles due to their optical contrast and even distribution throughout the model material. Shear strain rates are determined in Matlab by the gradient in the velocity field between each picture. The background strain rate of the machine is 10^{-3} s^{-1} and slip rates associated with stick-slip dynamics occur on the order of 10^{-2} s^{-1} and greater. Using these parameters and employing PIV, we can distinguish between continuous deformation of the Carbopol and slip on fractures.

3 Results

Based on patterns in the recorded force and displacement data, we can distinguish between stick-slip and creep dynamics as well as a mixture between these two cases (Figure 3). Stick-slip events are characterized by a period of locking and subsequent slip leading to a saw tooth pattern in the force data and a stair step pattern in the displacement data. During the locking period, the apparatus remains stationary while force continues to build. We observe a sharp drop in the force and a sudden increase in the displacement when the force is large enough to overcome the frictional resistance of the apparatus and the strength of the experimental material (Figure 3a). Slip dynamics in the continuum between stick-slip and creep exhibits a damped signal (Figure 3b). In these cases, the release of force takes place over a longer period of time (>5 s) compared to the stick-slip end member. Creep dynamics, on the other hand, lead to a continuous force and displacement curve with only minor oscillations (Figure 3c).

We perform a control experiment where we measure the signal of the empty machine before each experiment to ensure that it is constant over all experiments. The data for this benchmark experiment show a constant increase in displacement and a relatively constant force (Figure 4a). The force gauge has an instrumental noise amplitude of ±0.1 N. The frictional resistance of the apparatus' moving parts is responsible for the rest of the approximately 0.8 N oscillations. This background signal is present in all experiments.

The data from the 1 wt.% Carbopol experiments (yield stress = 25 Pa) show a creep signal with no sudden force drops (Figure 4b). Due to the damping effect of the Carbopol, we observe less noise in the force measurements compared to the benchmark experiment. We observe the formation of sets of parallel bands perpendicular to the direction of the compressive instantaneous stretching axis. A large band cross-cuts the pre-existing fracture without being offset by it (Figure 5a, b). This indicates that shear displacement is accommodated by distributed deformation rather than localized slip on the pre-existing fracture. We observe no fracture development during the experiment and all deformation is accommodated by ductile shear.

Experiments with 2 wt.% Carbopol (yield stress = 144 Pa) show a complex mixture of creep and stick-slip dynamics (Figure 4c). Initially, these experiments creep continuously with minor force oscillations (< 0.5 N amplitude). At approximately 100 seconds into the experiment, we start seeing a stick-slip signal. When shear strain approaches 0.5 (between 400 and 450 seconds), we observe a transition in which both damped stick-slip events and stick-slip events occur. In this transition, a prolonged damped stick-slip event (~10 s) occurs prior to three lower amplitude stick-slip events (~1 N) (Figure 4c, for detail see Figure 7). After 450 seconds, we record only damped stick-slip events and beyond 520 seconds, the signal returns to continuous creep.

We analyze the structural evolution in the experiments via photographs and PIV. At the intermediate yield stress, the rock analog both fractures and flows. Mode I fractures propagate as wing cracks from each tip of the pre-cut shear fracture as well as from the boundaries of the experiment (Figure 5c, d). From the velocity gradients across these fractures obtained by PIV, the slip rake can be calculated to highlight the fracture mode of active fractures (Figure 6). Here, slip rake or slip direction is represented by color and associated direction on the color wheel. For example, slip on a shear fracture that is parallel to the shear plane is colored red. Fractures highlighted in purple are extensional. The saturation of the color corresponds to the strain rate, which ranges between 0 and 0.01 s^{-1}. For example, at 462 seconds, we observe some shear deformation along the pre-existing fracture (Figure 6a). At 508 seconds, the wing cracks start to propagate from both tips of the shear fracture. During the opening of these mode I fractures we observe simultaneous shear deformation along the pre-existing shear fracture (Figure 6b). The opening of mode I fractures leads to a circular distortion of the velocity field at the fracture tips. At 552 seconds, the propagation of the wing cracks has halted and we observe only continuous extension along the mode I fractures. Some shear along the pre-existing fracture can still be observed (Figure 6c).

We use the velocity gradients to calculate the strain rate during deformation. Focusing on the transition from stick-slip to damped stick-slip in the 2 wt.% experiment, we investigate the fracture evolution associated with this transition (Figure 7). No localized deformation is observed while the experiment is locked (Figure 7b). After the slip event at approximately 380 seconds, the pre-existing shear fracture actively slips during a mixture of damped stick-slip and stick-slip events (Figure 7c). Once the mode I fractures begin to propagate (~0.2 mm/s), we no longer observe stick-slip events (Figure 7d). The interaction between the mode I fractures and the shear fracture leads to strain rates as high as 10^{-1} s^{-1}.

In contrast to the 1 and 2 wt.% Carbopol experiments, stick-slip is dominant in 3 wt.% Carbopol (yield stress = 357 Pa) experiments (Figure 4d). The force data shows a clear saw tooth pattern while the displacement data exhibits a characteristic stair-step pattern. We observe the formation of abundant mode I fractures that initialize on the pre-existing shear fracture as well as from the interior and edges of the experiment (Figure 5e, f). Over the course of the experiment, the slab of Carbopol gets increasingly segmented due to fractures that swiftly propagate (~2 mm/s) across the entire width of the experiment. We analyze the PIV strain field in the same interval as the 2 wt.% experiment (Figure 8). The propagation of mode I fractures can be observed during both locking and slip while we do not observe slip on the pre-existing shear fracture at all (Figure 8a, b). The deformation is predominantly accommodated by the opening of mode I fractures. A mode I fracture is shown propagating (black circles) during both a period of locking and slip (Figure 8b, c). Because the 3 wt.% Carbopol has a high yield stress, deformation is able to localize at any heterogeneity, including the individual strips of the moving table (Figure 8b, c).

To illustrate the effect of the yield stress on deformation, we compare the displacement data of each of the experiments by setting the displacement at t = 350 s to 0 cm (Figure 9). While the 1 wt.% Carbopol deforms entirely by continuous creep and the 3 wt.% experiment deforms by stick-slip, the slip dynamics of the 2 wt.% Carbopol exhibits a spectrum between stick-slip and creep. The slopes during the force increase of damped stick-slip events in the 2 wt.% experiment are comparable to the continuous creep in the 1 wt.% experiments. We calculate the instantaneous slip rates (peak velocity) of each slip event by using the derivative of the displacement curves (Figure 9 inset). The slip events themselves have on average less steep slopes and lower average slip rates (0.8 mm/s and 1.4 mm/s, respectively) when compared to the 3 wt.% experiment (Figure 9). In the 3 wt.% experiments the instantaneous slip rates are twice as high on average compared to the 2 wt.% experiment (2 mm/s and 4 mm/s, respectively).

4 Discussion

Our results show that the yield stress of the material controls the fracture dynamics, which further impacts the slip dynamics. Besides the variability in the force and displacement data we also observe variations in fracture patterns depending on the yield stress. The number of fractures increases with an increasing yield stress, but the impact of the fracture formation on the slip dynamics is not straight forward. Multiple fractures can form and propagate at the same time within one experiment. The force and displacement measurements, however, record only bulk behavior. This makes connecting the opening of one specific fracture to one specific slip event non-trivial. Furthermore, different types of fractures (mode I and II) can interact during an experiment impacting the dynamics. In the absence of fracture development, we observe creep motion. While the development of mode I fractures coincides with stick-slip and damped stick-slip events we can also observe a stick-slip signal when there is shear along the pre-existing mode II fracture. We only observe damped stick-slip events in experiments where mode I and the pre-existing shear fracture interact (Figure 7). When mode I fractures are not interacting with the shear fracture we observe stick-slip (Figure 8). This indicates that the recorded stick-slip signal has two potential sources. 1) It can originate from movement on the pre-existing shear fracture, because of frictional sliding on the existing surface (Scholz 1990). Or 2) it can result from the opening of mode I fractures similar to observations reported by Reber et al. (2015). A low yield stress (25 Pa) leads to creep dynamics in the absence of fractures. An intermediate yield stress (144 Pa) leads to the development of some mode I fractures, which interact with the pre-existing shear fracture. This produces a spectrum in slip dynamics ranging from creep to damped stick-slip to stick-slip. A high yield stress (357 Pa) results in the development of many mode I fractures and a clear stick-slip signal.

The speed of the mode I fracture propagation is dependent on the material's yield stress. High yield stress experiments develop many fast propagating fractures that rapidly segment and weaken the material. In intermediate yield stress experiments, the mode I fractures propagate from the introduced perturbation of the slipping pre-existing shear fracture. In comparison to high yield stress experiments the propagation speed of mode I fractures is slower. The fracture propagation speed is directly dependent on the yield stress and therefore the concentration between the brittle and viscous phases in Carbopol. The presence of the viscous phase is responsible for the dampening of the fracture propagation speed. In cases where the concertation of the brittle phase is too low, no fractures can develop and all deformation is accumulated in a ductile manner (Di Giuseppe et al., 2015; Shafiei et al., 2018).

Experiments can be considered in an analogy-based framework or in an analytical framework (Paola et al., 2009) In an analogy-based framework, an experiment is an analog for nature and treating the experiment as a classically scaled model is unavoidable. The experiments presented here were conducted in an analytical frame work. In this framework, experiments need to capture enough of the relevant dynamics to serve as a plausible test of the problem at hand (Paola et al., 2009). We argue that the rheological similarity between mid-crustal mineral assemblages (e.g. Hayman and Lavier, 2014; Handy, 1990) and Carbopol provides the necessary similarity to test the impact of a visco-elasto-plastc rheology, and especially the yield stress, on deformation patterns and dynamics. Thus, although the results presented here cannot simply be up-scaled to natural rock deformation, we are able to make in situ observations of physical processes that lead to various slip-dynamics in a material that exhibits semi-brittle deformation, which in all likelihood has implications for similar natural systems.

5 Implications for Natural Systems

Several field (Fagereng and Sibson, 2010; Handy, 1990) and numerical (Jammes et al., 2015; Webber et al., 2018) studies have indicated that the brittle to viscous phase ratio controls the type of deformation. This can lead to three different deformation styles: (1) the strong, brittle phase provides a stress supporting framework leading to dominantly brittle deformation, (2) rheology is controlled by the flow of the weak, ductile phase where stronger asperities are isolated, and (3) where both phases accommodate strain by a mixture of localized brittle failure and ductile flow (Figure 1). We can simulate all three deformation styles by changing yield stress values in our experiments. Low brittle to viscous phase ratios, as in our 1 wt.% experiments, favor continuous deformation. With an intermediate brittle to viscous ratio, deformation exhibits a combination of strain localization and viscous flow (2 wt.% experiment). For a high brittle to viscous phase ration (3 wt.% experiment) deformation is predominantly brittle. A change in the ratio between brittle and viscous phases could also be viewed as a proxy for the impact of temperature on the rock rheology. In rocks, the relative strength of mineral phases is controlled by pressure and temperature conditions (Ellis, 1988), where an increase in temperature leads to a more viscous behavior. Jammes et al. (2015) investigated the combined effects of quartz to feldspar ratios and temperature conditions on the localization and distribution of shear. At low temperatures the deformation style was localized and resembled cataclasis whereas at high temperatures the deformation was widely distributed. Localization decreased with an increase in abundance of quartz. This indicates that the bulk strength is influenced by both temperature and relative phase abundance. In our experiments, we do not control for pressure nor temperature. The three yield stress values of Carbopol chosen are, however, representative of both the change in phase ratio in rock but also the change in temperature with depth. The 3 wt.% Carbopol represents rock near the shallow end of the semi-brittle regime where deformation is predominantly brittle. The 1 wt.% experiment represents the deepest part of the semi-brittle zone where slip approaches aseismic ductile creep.

In our experiments, we observe a continuum between creep and stick-slip. By increasing the relative proportion of the viscous phase in Carbopol and therefore lowering the yield stress, we see a decrease in slip speed and number of slip events approaching creep (Figure 9). We suggest that the observed continuum of slip behavior directly relates to the change in bulk strength in rock with depth. Wech and Creager (2011) analyzed patterns in slow slip events (SSE) in the Cascadia subduction zone where they made similar observations. Their findings show that fault slip near the base of the seismogenic zone favored larger and infrequent slip events compared to increased depths where smaller, more frequent slip events begin to approach continuous creep of the entirely ductile crust (see Figure 3 in Wech and Creager (2011)). While they argue that pore fluid pressure is the controlling factor for this transition we suggest that the bulk yield stress might lead to a similar transition from stick-slip to creep and that it may be an additional mechanism.

6 Conclusion

We conducted experiments using Carbopol of three different yield stresses deformed by simple shear. The experiments show a direct correlation between the Carbopol's yield stress, the fracture formation, and the slip dynamics. A high yield stress leads to the formation of abundant mode I fractures and to stick-slip deformation dynamics. A low yield stress results in continuous viscous creep in the absence of fractures. We observe dynamics of both stick-slip and creep in experiments with an intermediate yield stress. The interplay of mode I fractures and the pre-existing shear fracture leads to a damped stick-slip signal. Our results suggest that a stick-slip-like signal can originate not only from frictional sliding on an existing surface but also due to the opening and interactions of fractures during shear deformation. The fracture patterns and resulting deformation dynamics are governed by the yield stress. We further suggest that bulk yield stress may be an important variable controlling the continuum from creep to stick-slip in natural faults.

Acknowledgements

We thank Neil Mancktelow and Alexandra Hatem for their thoughtful comments and helpful suggestions. TB and JER were supported by NSF grant EAR-1547492. Special thanks to Kevin Toeneboehn and Michele Cooke for help in developing Matlab codes for use in this study.

Data presented in the results and supplemental information is freely available through DataShare: the Open Data Repository of Iowa State University (https://doi.org/10.25380/iastate.7746635).

References

Beroza, G. C., and S. Ide (2011), Slow Earthquakes and Nonvolcanic Tremor, *Annu Rev Earth Pl Sc*, *39*, 271-296, doi:10.1146/annurev-earth-040809-152531.

Burgmann, R. (2018), The geophysics, geology and mechanics of slow fault slip, *Earth Planet Sc Lett*, *495*, 112-134, doi:10.1016/j.epsl.2018.04.062.

Burgmann, R., D. Schmidt, R. M. Nadeau, M. d'Alessio, E. Fielding, D. Manaker, T. V. McEvilly, and M. H. Murray (2000), Earthquake potential along the northern Hayward fault, California, *Science*, *289*(5482), 1178-1182, doi:10.1126/science.289.5482.1178.

Burton, J. C., J. M. Amundson, R. Cassotto, C. C. Kuo, and M. Dennin (2018), Quantifying flow and stress in ice melange, the world's largest granular material, *P Natl Acad Sci USA*, *115*(20), 5105-5110, doi:10.1073/pnas.1715136115.

Carreras, J. (2001), Zooming on Northern Cap de Creus shear zones, *J Struct Geol*, *23*(9), 1457-1486, doi:10.1016/S0191-8141(01)00011-6.

Coussot, P., L. Tocquer, C. Lanos, and G. Ovarlez (2009), Macroscopic vs. local rheology of yield stress fluids, *J Non-Newton Fluid*, *158*(1-3), 85-90, doi:10.1016/j.jnnfm.2008.08.003.

Di Giuseppe, E., F. Corbi, F. Funiciello, A. Massmeyer, T. N. Santimano, M. Rosenau, and A. Davaille (2015), Characterization of Carbopol hydrogel rheology for experimental tectonics and geodynamics, *Tectonophysics*, *642*, 29-45, doi:10.1016/j.tecto.2014.12.005.

Ellis, M. (1988), Lithospheric strength in compression - Initiation of subduction, flake tectonics, foreland migration of thrusting, and an origin of displaced terranes, *J. Geol.*, *96*(1), 91-100, doi:10.1086/629195.

Fagereng, A., and C. Harris (2014), Interplay between fluid flow and fault-fracture mesh generation within underthrust sediments: Geochemical evidence from the Chrystalls Beach Complex, New Zealand, *Tectonophysics*, *612*, 147-157, doi:10.1016/j.tecto.2013.12.002.

Fagereng, A., and R. H. Sibson (2010), Melange rheology and seismic style, *Geology*, *38*(8), 751-754, doi:10.1130/G30868.1.

Fitz Gerald, J. D., and H. Stunitz (1993), Deformation of Granitoids at Low Metamorphic Grade .1. Reactions and Grain-Size Reduction, *Tectonophysics*, *221*(3-4), 269-297, doi:10.1016/0040-1951(93)90163-E.

Gapais, D. (1989), Shear Structures within Deformed Granites - Mechanical and Thermal Indicators, *Geology*, *17*(12), 1144-1147, doi:10.1130/0091-7613(1989)017<1144:Sswdgm>2.3.Co;2.

Handy, M. R. (1990), The Solid-State Flow of Polymineralic Rocks, *J Geophys Res-Solid*, *95*(B6), 8647-8661, doi:10.1029/JB095iB06p08647.

Hayman, N. W., and L. L. Lavier (2014), The geologic record of deep episodic tremor and slip, *Geology*, *42*(3), 195-198, doi:10.1130/G34990.1.

Higashi, N., and I. Sumita (2009), Experiments on granular rheology: Effects of particle size and fluid viscosity, *J Geophys Res-Sol Ea*, *114*, doi: 10.1029/2008jb005999.

Jammes, S., L. L. Lavier, and J. E. Reber (2015), Localization and delocalization of deformation in a bimineralic material, *J Geophys Res-Sol Ea*, *120*(5), 3649-3663, doi:10.1002/2015jb011890.

Kanamori, H. (1994), Mechanics of Earthquakes, *Annu. Rev. Earth Planet. Sci.*, *22*, 207-237, doi:10.1146/annurev.ea.22.050194.001231.

Lavier, L. L., R. A. Bennett, and R. Duddu (2013), Creep events at the brittle ductile transition, *Geochem Geophy Geosy*, *14*(9), 3334-3351, doi:10.1002/ggge.20178.

Lubrizol (2012), Neutralizing Carbopol and Pemulen Polymers in Aqueous and Hydroalcoholic Systems, *Lubrizol Technical Data Sheet 237*, 1-4.

Mancktelow, N. S. (2006), How ductile are ductile shear zones, *Geology*, 34(5), 345–348, doi:10.1130/G22260.1

Mancktelow, N. S. (2008), Interaction between brittle fracture and ductile flow during crustal deformation, *B Soc Geol Ital*, *127*(2), 217-220.

Mancktelow, N. S., and G. Pennacchioni (2005), The control of precursor brittle fracture and fluid-rock interaction on the development of single and paired ductile shear zones, *J Struct Geol*, *27*(4), 645-661, doi:10.1016/j.jsg.2004.12.001.

Moore, P. L. (2014), Deformation of debris-ice mixtures, *Rev Geophys*, *52*(3), 435-467, doi:10.1002/2014rg000453.

Nevitt, J. M., J. M. Warren, and D. D. Pollard (2017), Testing constitutive equations for brittle-ductile deformation associated with faulting in granitic rock, *J. Geophys. Res. Solid Earth*, 122(8), 6269–6293, doi:10.1002/2017JB014000.

Paola, C., K. Straub, D. Mohrig, and L. Reinhardt (2009), The "unreasonable effectiveness" of stratigraphic and geomorphic experiments, Earth-Sci Rev, 97(1-4), 1-43, doi:10.1016/j.earscirev.2009.05.003.

Peng, Z. G., and J. Gomberg (2010), An integrated perspective of the continuum between earthquakes and slow-slip phenomena, *Nat Geosci*, *3*(9), 599-607, doi:10.1038/Ngeo940.

Pennacchioni, G., and N. S. Mancktelow (2013), Initiation and growth of strike-slip faults within intact metagranitoid (Neves area, eastern Alps, Italy), *Geol Soc Am Bull*, *125*(9-10), 1468-1483, doi:10.1130/B30832.1.

Piau, J. M. (2007), Carbopol gels: Elastoviscoplastic and slippery glasses made of individual swollen sponges Meso- and macroscopic properties, constitutive equations and scaling laws, *J Non-Newton Fluid*, *144*(1), 1-29, doi:10.1016/j.jnnfm.2007.02.011.

Reber, J. E., N. W. Hayman, and L. L. Lavier (2014), Stick-slip and creep behavior in lubricated granular material: Insights into the brittle-ductile transition, *Geophys Res Lett*, *41*(10), 3471-3477, doi:10.1002/2014gl059832.

Reber, J. E., L. L. Lavier, and N. W. Hayman (2015), Experimental demonstration of a semi-brittle origin for crustal strain transients, *Nat Geosci*, *8*(9), 712-716, doi:10.1038/Ngeo2496.

Scholz, C. H. (1990), Geophysics - Earthquakes as Chaos, Nature, 348(6298), 197-198, doi: 10.1038/348197a0.

Schreurs, G. (1994), Experiments on Strike-Slip Faulting and Block Rotation, Geology, 22(6), 567-570, doi:10.1130/0091-7613(1994)022<0567:Eossfa>2.3.Co;2.

Shafiei, M., M. Balhoff, and N. W. Hayman (2018), Chemical and microstructural controls on viscoplasticity in Carbopol hydrogel, *Polymer*, *139*, 44-51, doi:10.1016/j.polymer.2018.01.080.

Simpson, C. (1985), Deformation of Granitic-Rocks across the Brittle Ductile Transition, *J Struct Geol*, *7*(5), 503-511, doi: 10.1016/0191-8141(85)90023-9.

Stunitz, H., and J. D. Fitz Gerald (1993), Deformation of Granitoids at Low Metamorphic Grade .2. Granular Flow in Albite-Rich Mylonites, *Tectonophysics*, *221*(3-4), 299-324, doi:10.1016/0040-1951(93)90164-F.

Tabuteau, H., S. Mora, M. Ciccotti, C. Y. Hui, and C. Ligoure (2011), Propagation of a brittle fracture in a viscoelastic fluid, *Soft Matter*, *7*(19), 9474-9483, doi:10.1039/c1sm06024d.

Thatcher, W. (2009), How the Continents Deform: The Evidence From Tectonic Geodesy, *Annu. Rev. Earth Planet. Sci.*, *37*, 237-262, doi:10.1146/annurev.earth.031208.100035.

Thielicke, W. and Stamhuis, E.J. (2014a): PIVlab – Towards User-friendly, Affordable and Accurate Digital Particle Image Velocimetry in MATLAB. *Journal of Open Research Software* 2(1):e30, doi: 10.5334/jors.bl

Thielicke, W., and E. J. Stamhuis (2014b), PIVlab - Time-Resolved Digital Particle Image Velocimetry Tool for MATLAB (version:1.31), doi:http://dx.doi.org/10.6084/m9.figshare.1092508

Thielicke, W. (2014): The Flapping Flight of Birds - Analysis and Application. Phd thesis, Rijksuniversiteit Groningen. http://irs.ub.rug.nl/ppn/382783069

Viegas, G., L. Menegon, and C. Archanjo (2016), Brittle grain-size reduction of feldspar, phase mixing and strain localization in granitoids at mid-crustal conditions (Pernambuco shear zone, NE Brazil), *Solid Earth*, *7*(2), 375-396, doi:10.5194/se-7-375-2016.

Webber, S., S. Ellis, and A. Fagereng (2018), "Virtual shear box" experiments of stress and slip cycling within a subduction interface melange, *Earth Planet Sc Lett*, *488*, 27-35, doi:10.1016/j.epsl.2018.01.035.

Wech, A. G., and K. C. Creager (2011), A continuum of stress, strength and slip in the Cascadia subduction zone, *Nat Geosci*, *4*(9), 624-628, doi:10.1038/ngeo1215.

Figure 1. Schematic "Christmas tree" diagram of mineral flow laws in granitoid rock illustrating the transition from brittle to semi-brittle to ductile bulk deformation. Modified from Jammes et al. (2015) and Nevitt et al. (2017).

Figure 2. 3-D diagram of the simple shear apparatus. A stepper motor drives the moving side at a constant velocity. The motor is attached to a force gauge (F(t) in inset) that is linked to the apparatus by a spring. x(t) measures the position of the moving side of the table.

Figure 3. Examples of different slip types. Raw data from 2 wt.% experiments for stick-slip and damped stick-slip. Continuous creep is shown in data from 1 wt.% experiments.

Figure 4. Unfiltered force and displacement data from representative experiments. The force curve is shown in red and the displacement curve in green. σ_y is the yield stress.

Figure 5. Photos and sketches of experiments at $\gamma = 1$. Direction of shear is top to the right. **a, b)** 1 wt.% Carbopol with bands present. **c, d)** 2 wt.% Carbopol with fracture void space sketched in black. **e, f)** 3 wt.% Carbopol. Inactive mode II fractures are indicated by a dashed line.

Figure 6. Slip rake of 2 wt.% Carbopol. The color wheel legend shows strain rate (s^{-1}) shown by the saturation in color. Slip rake is identified by color with direction shown on the color wheel (Red = shear slip, purple = extension, and green = compression). **a)** Active strike-slip motion on the pre-existing shear fracture. **b)** Propagation of mode I fractures (wing cracks). **c)** Opening and shear slip occurring simultaneously.

Figure 7. a) Zoom in on force and displacement data of 2 wt.% Carbopol. Elliptical IIR filtered data is shown in color and raw data in gray. **b)** No localization of deformation is visible in the strain field. **c)** At 400 seconds, some shear deformation along the pre-existing fracture. **d)** At 500 seconds, the wing cracks start to propagate from both tips of the shear fracture.

Figure 8. a) Zoom in on force and displacement data of 3 wt.% Carbopol. Elliptical IIR filtered data is shown in color and raw data in gray. **b)** Propagation of mode I fracture (black circle) from the pre-existing shear fracture (dashed line). There is no detectable slip on the shear fracture. Additional fractures are propagating form the edges. **c)** Further propagation of mode I fracture (circle) without slip on the shear fracture.

Figure 9. Comparison of slip kinematics between 1,2, and 3 wt.% Carbopol. **a)** Normalized displacement curves are set to zero at t = 350 s. **b)** Box plot of slip speeds. In box plots the blue boxes are centered on the mean velocities. The top and bottom of the box are one standard deviation from the mean. The black whiskers are two standard deviations from the mean. Red plus signs indicate slip events that are more than two standard deviation from the mean. The red horizontal bars represent median slip velocities.

Figure 1.

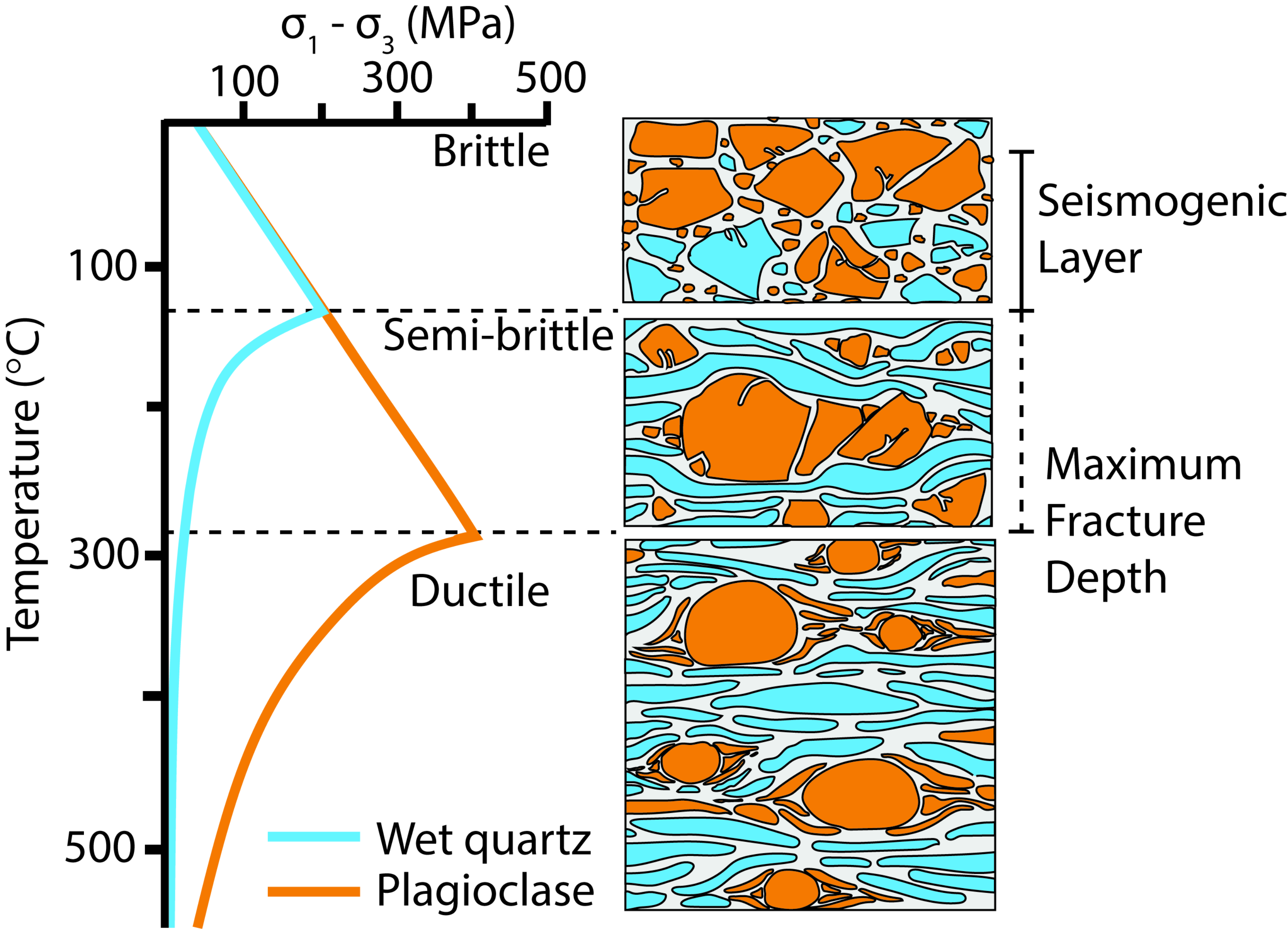

σ1 - σ3 (MPa)
100
300
500
Brittle
Semi-brittle
Ductile
Temperature (°C)
100
300
500
Wet quartz
Plagioclase
Seismogenic Layer
Maximum Fracture Depth

Figure 2.

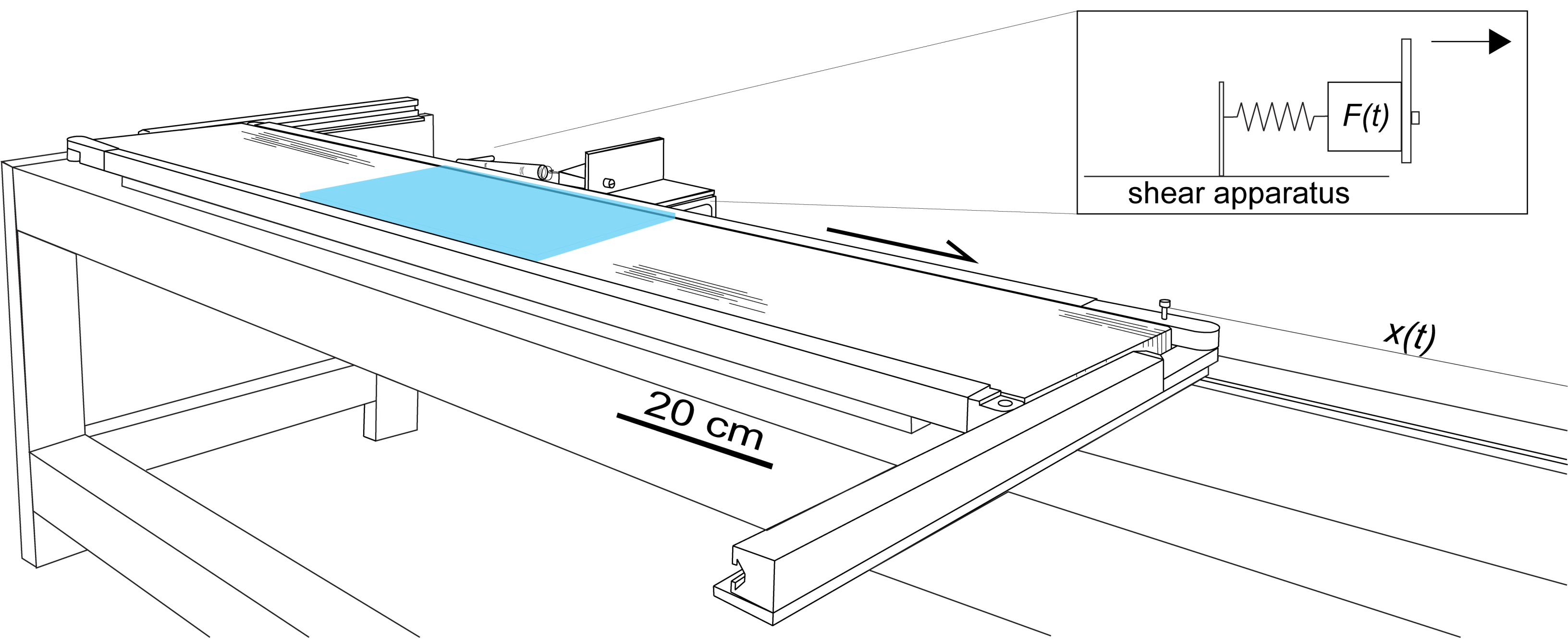

F(t)
shear apparatus
x(t)
20 cm

Figure 3.

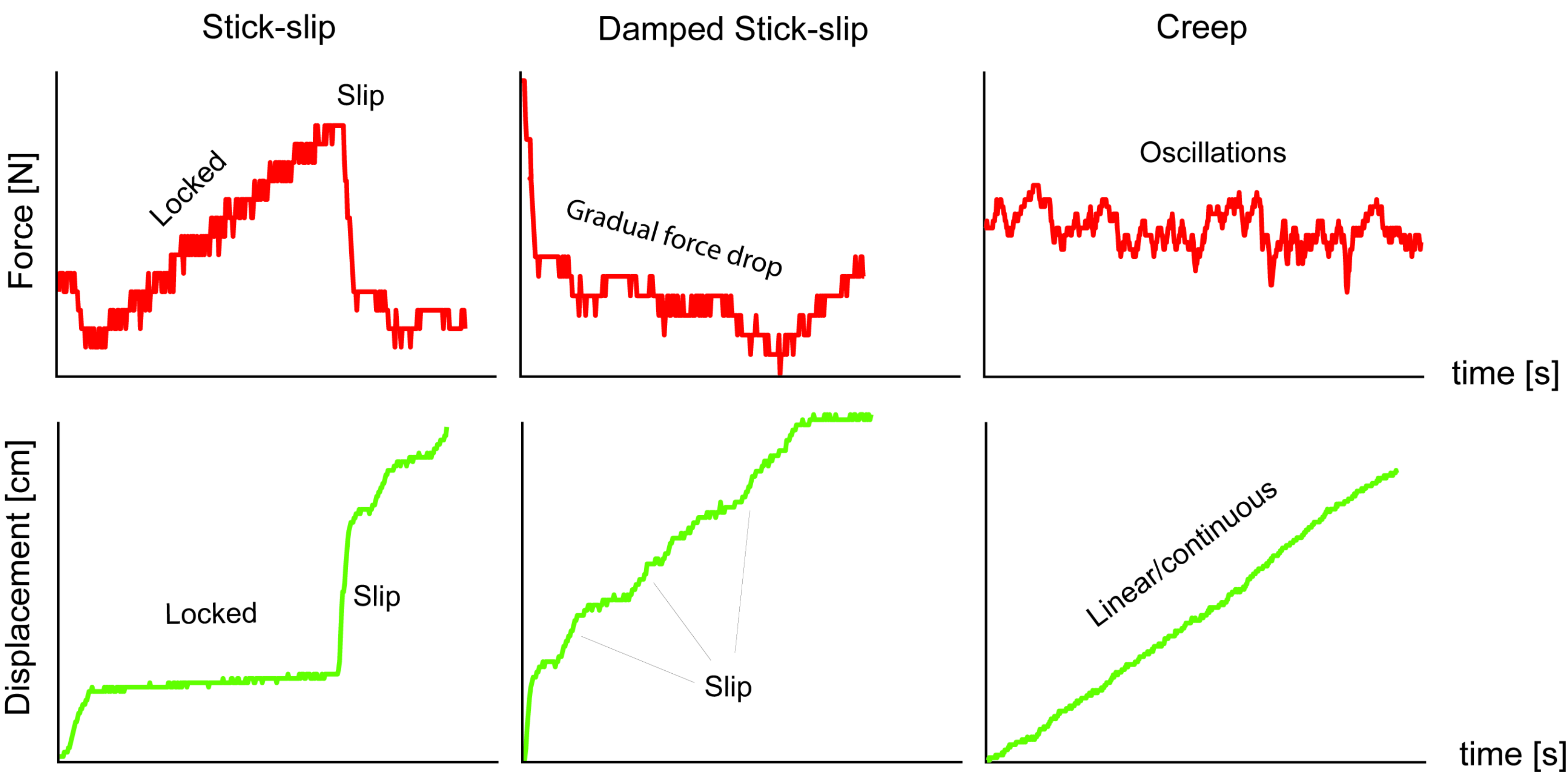
Stick-slip
Damped Stick-slip
Creep
Force [N]
Slip
Locked
Gradual force drop
Oscillations
time [s]
Displacement [cm]
Locked
Slip
Slip
Linear/continuous
time [s]

Figure 4.

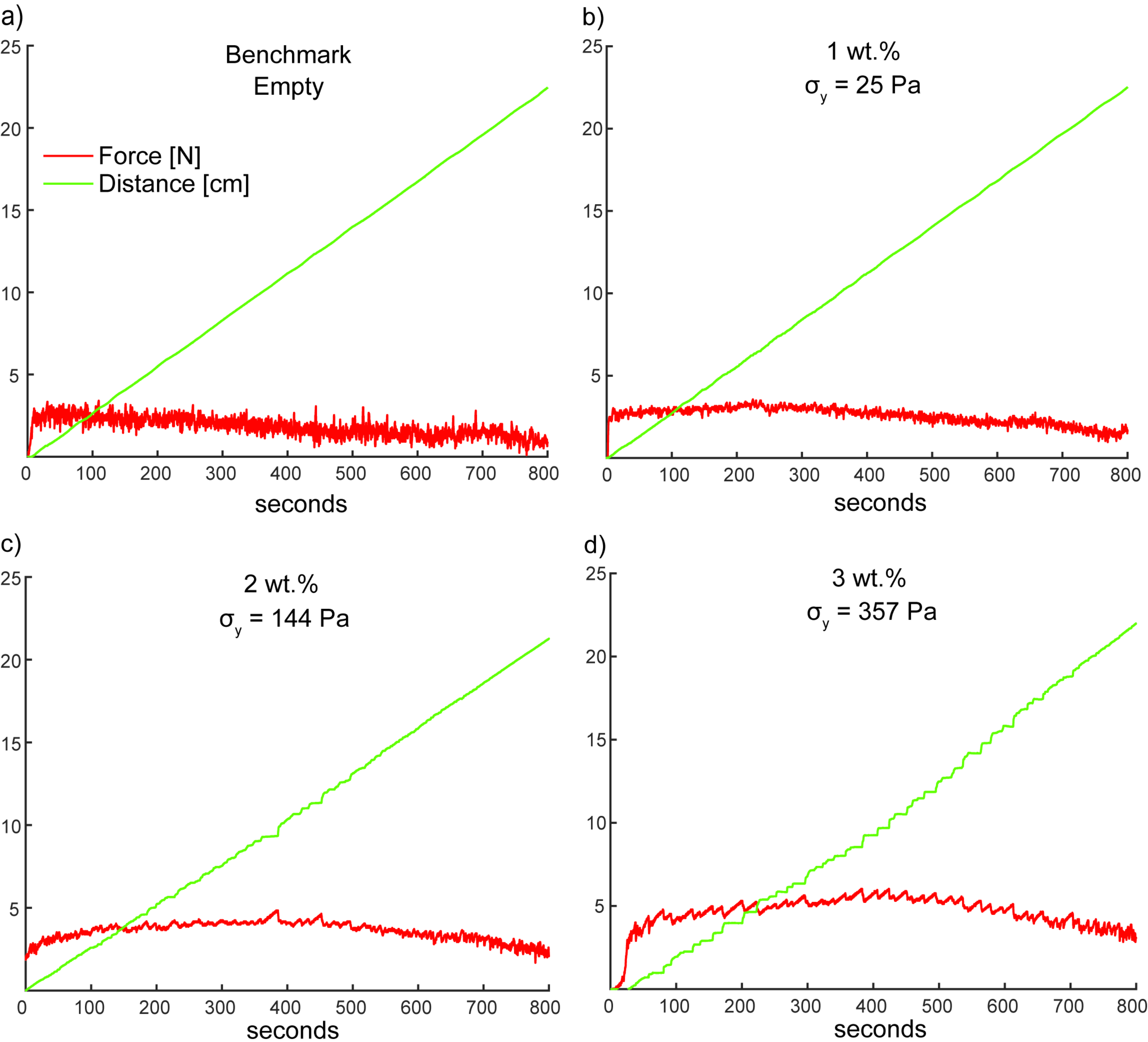
a)
Benchmark
Empty
Force [N]
Distance [cm]
seconds
b)
1 wt.%
σy = 25 Pa
seconds
c)
2 wt.%
σy = 144 Pa
seconds
d)
3 wt.%
σy = 357 Pa
seconds

Figure 5.

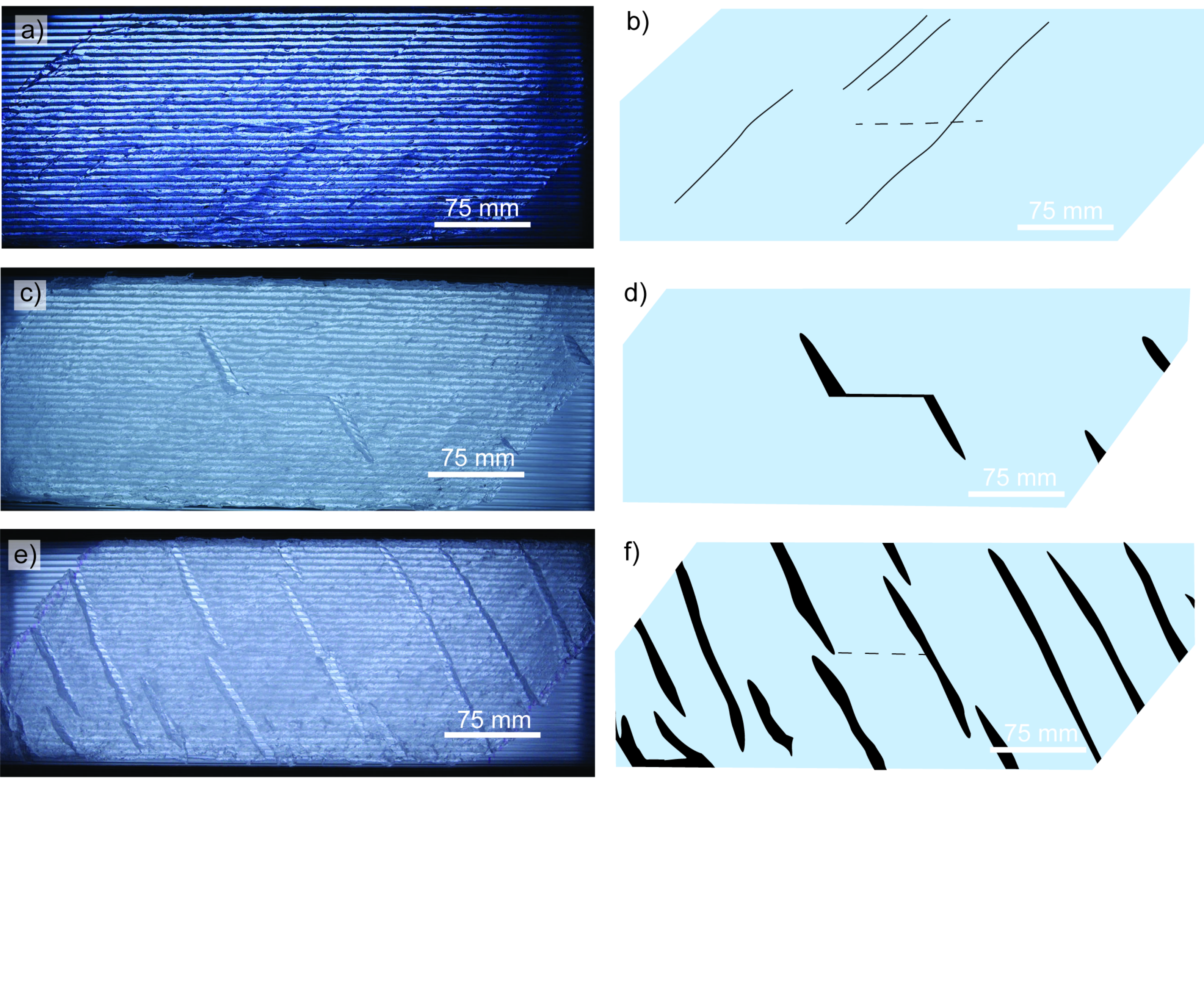
a)
75 mm
b)
75 mm
c)
75 mm
d)
75 mm
e)
75 mm
f)
75 mm

Figure 6.

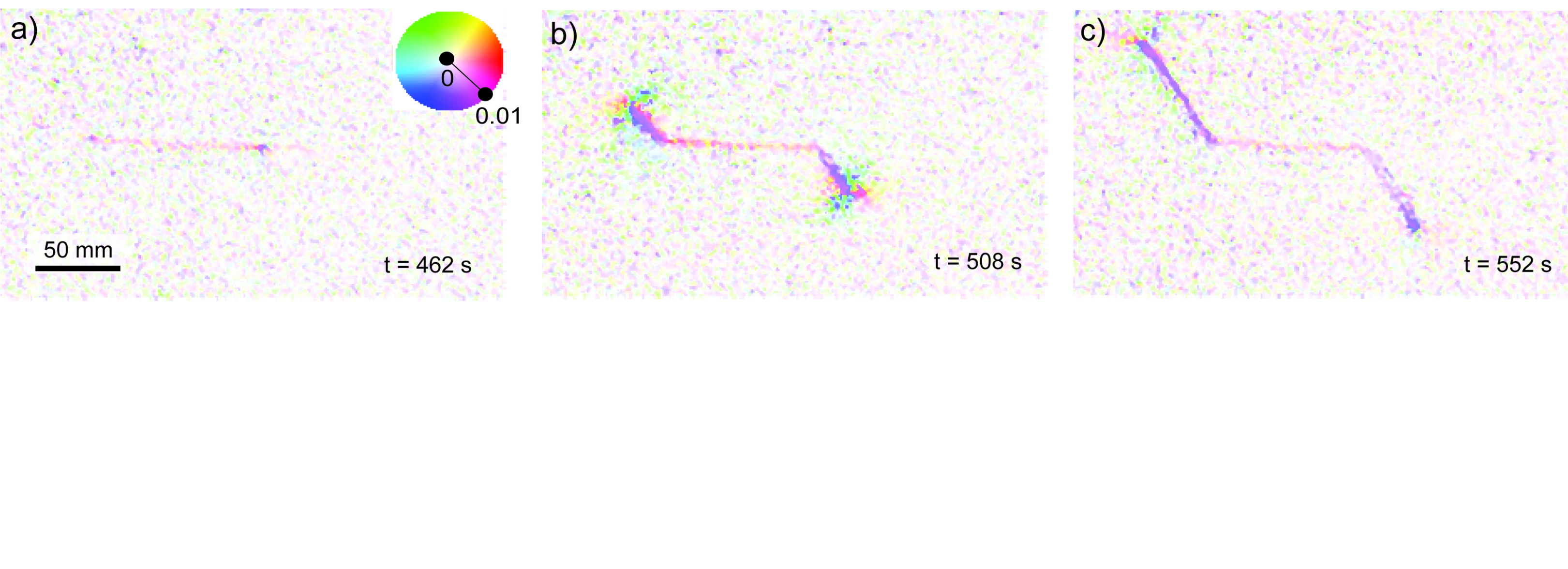

a)
0
0.01
50 mm
t = 462 s
b)
t = 508 s
c)
t = 552 s

Figure 7.

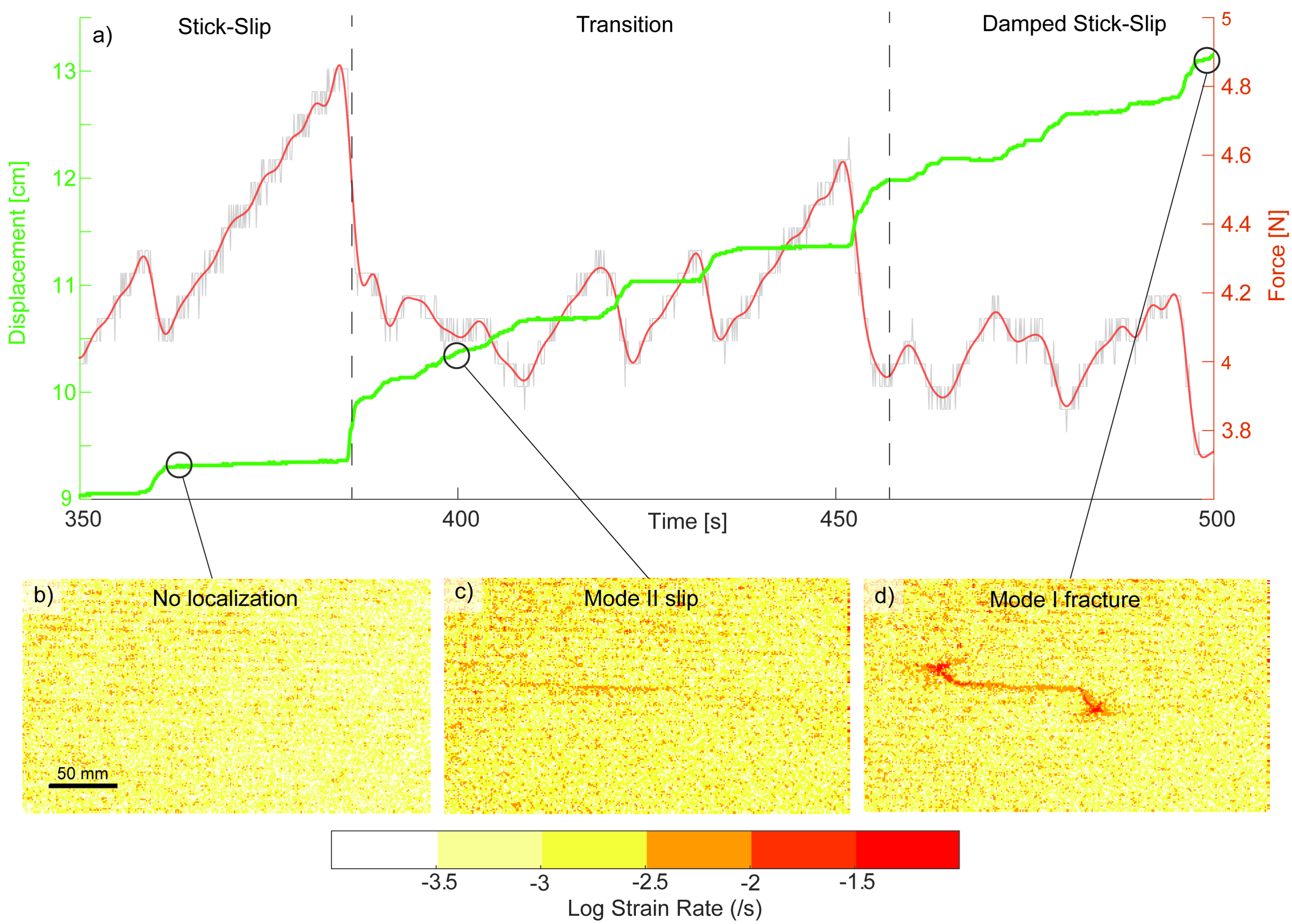
a)
Stick-Slip
Transition
Damped Stick-Slip
Displacement [cm]
Force [N]
Time [s]
b)
No localization
50 mm
c)
Mode II slip
d)
Mode I fracture
Log Strain Rate (/s)
-3.5
-3
-2.5
-2
-1.5

Figure 8.

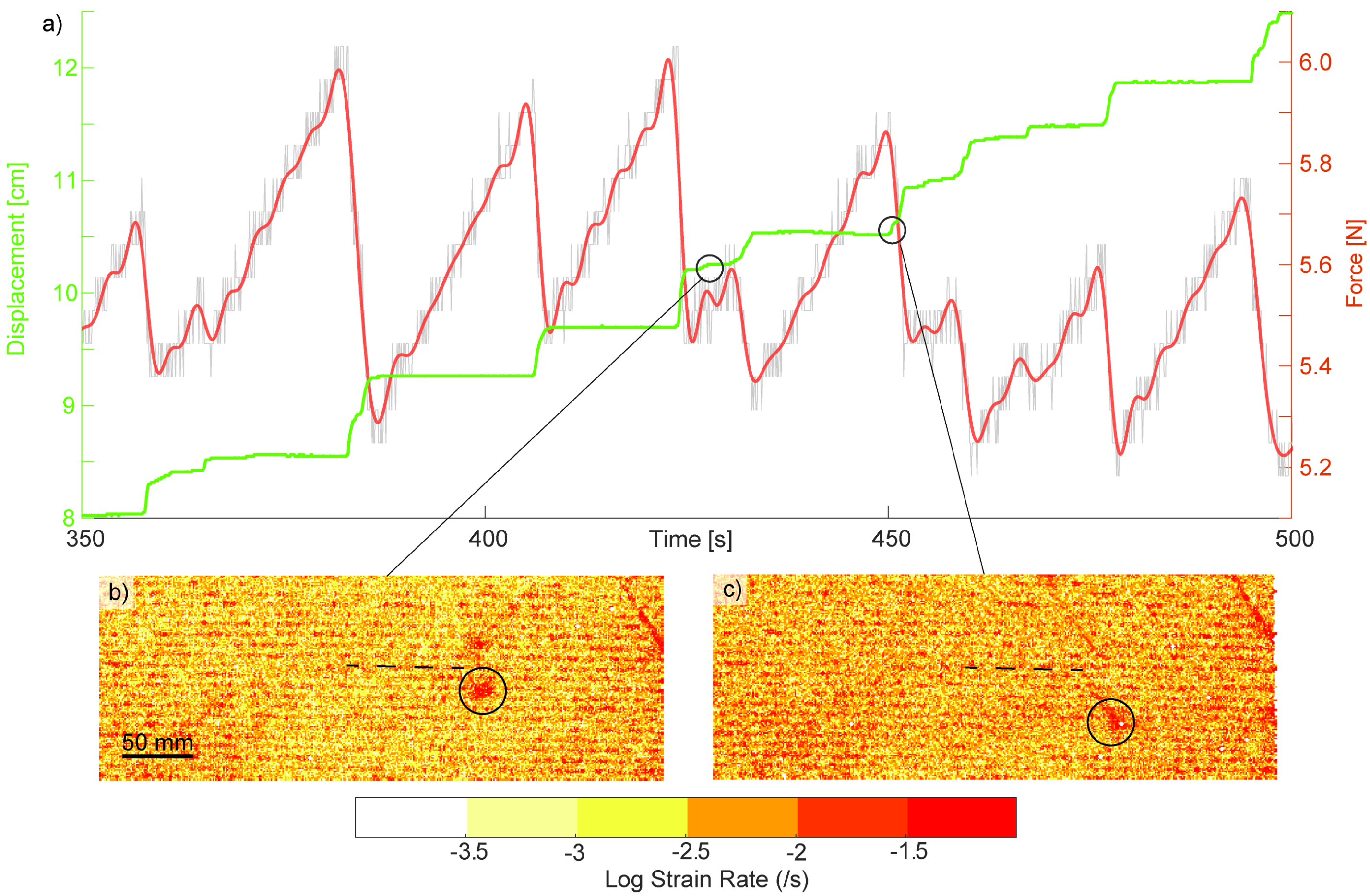

a)
Displacement [cm]
Force [N]
Time [s]
350
400
450
500
8
9
10
11
12
5.2
5.4
5.6
5.8
6.0
b)
c)
50 mm
-3.5
-3
-2.5
-2
-1.5
Log Strain Rate (/s)

Figure 9.

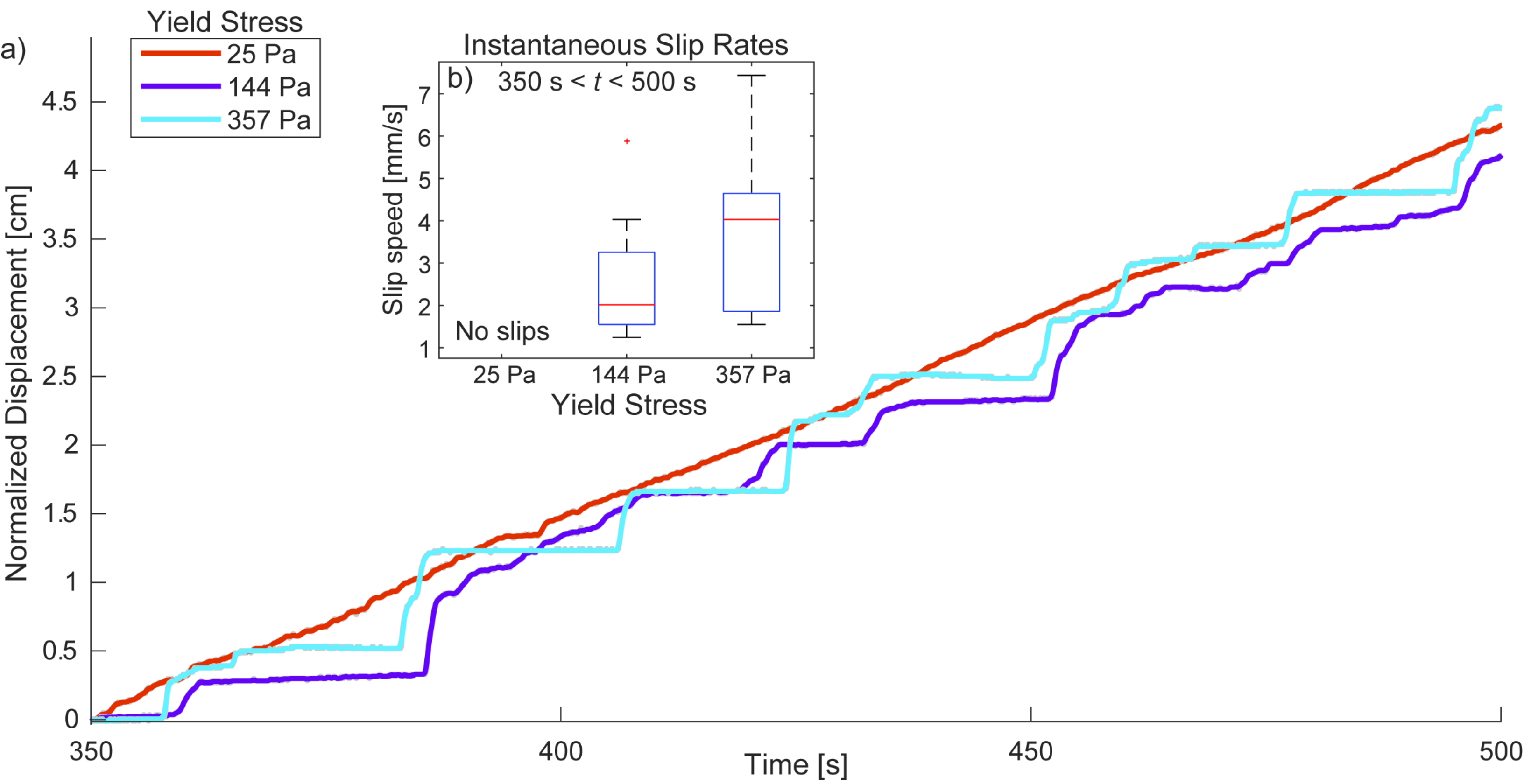
a)
Yield Stress
25 Pa
144 Pa
357 Pa
Normalized Displacement [cm]
Time [s]
Instantaneous Slip Rates
b) 350 s < t < 500 s
Slip speed [mm/s]
No slips
25 Pa
144 Pa
357 Pa
Yield Stress